Available online at www.sciencedirect.com
SCIENCE DIRECT®
Computers and Structures 83 (2005) 1366–1385
Computers & Structures
www.elsevier.com/locate/compstruc

New approximations and collocation schemes in the finite cloud method

Xiaozhong Jin [a], Gang Li [b], N.R. Aluru [a,*]

[a] Department of Mechanical and Industrial Engineering, University of Illinois at Urbana-Campaign, Beckman Institute for Advanced Science and Technology, 405 North Mathews Avenue, Urbana, IL 61801, United States
[b] Beckman Institute, UIUC, United States

Accepted 8 October 2004
Available online 9 March 2005

Abstract

The finite cloud method (FCM) [Int. J. Numer. Methods in Eng. 50(10) (2001) 2373] is a meshless technique combining a fixed kernel approximation of the unknown function(s) with a point collocation discretization of the governing PDEs. The meshless approximation and the collocation discretization are the two major steps in FCM. Since the quality of the numerical solution depends on the quality of the meshless approximation functions or shape functions and the discretization scheme employed, in this paper, we propose several improvements to the construction of meshless shape functions and compare several collocation schemes within the framework of the FCM. The improvements to the shape functions are combined with various collocation schemes to solve several 2-D Poisson and elastostatic examples. The convergence characteristics of the collocation schemes are studied. The accuracy of the collocation schemes with a scattered point distribution is also investigated.

Keywords: Finite cloud method; Fixed reproducing kernel approximation; Point collocation; Strong form integration; Least-squares collocation; Double grid collocation; Meshless method

1. Introduction

Meshless methods have emerged as a class of effective numerical methods which are capable of avoiding the difficulties encountered in conventional computational mesh based methods, such as, meshing complex geometries, mesh distortion due to large deformation and remeshing in moving boundary problems. Extensive research has been conducted in the area of meshless methods in recent years (see [2–4] for an overview). Broadly defined, meshless methods contain two key steps: construction of meshless approximation functions or shape functions and their derivatives and meshless discretization of the governing partial-differential equations (PDEs). Least-squares, kernel-based and radial basis function approaches are three techniques that have gained considerable attention for construction of meshless shape functions. The meshless discretization of the partial-differential equations can be categorized into three classes: cell integration, local point integration, and point collocation. A more detailed review of these techniques is presented in [5].

* Corresponding author. Tel.: +1 217 3331180; fax: +1 217 2444333.
E-mail address: aluru@uiuc.edu (N.R. Aluru).
URL: http://www.uiuc.edu/~aluru (N.R. Aluru).

0045-7949/$ - see front matter © 2005 Elsevier Ltd. All rights reserved.
doi:10.1016/j.compstruc.2004.08.030

The finite cloud method (FCM) [1] is a meshless method combining a fixed kernel approximation of the unknown function(s) with a point collocation discretization of the governing PDEs. Least-squares and kernel-based approaches have been used extensively for the construction of meshless shape functions (see [6] for a detailed discussion on the similarity between least-squares and kernel approximations). However, several limitations exist in the standard kernel and least-squares approaches:

1. The shape functions do not have the Kronecker delta property. In a global weak form discretization approach, this can impose difficulty and require more computational effort in enforcing the essential boundary conditions [14]. Moreover, it has been shown that [13], for approximations with a polynomial basis and second-order consistency conditions, the Kronecker delta property is a necessary and sufficient condition for satisfying the first positivity condition in a meshless point collocation approach. Various techniques [15–18] have been proposed in the literature to overcome this difficulty. However, the implementation of these techniques can be involved.
2. The construction of the meshless shape functions treats the boundary and the interior nodes the same way and, typically, the boundary conditions and the governing equations are not satisfied simultaneously at the boundary; satisfying the boundary conditions and the governing equations simultaneously at the boundary can provide a more accurate solution to a given problem.
3. For structures with a high aspect ratio, it is desirable to reduce the number of points along the dimension with a larger length. Unfortunately, analogous to the "locking" phenomena in the finite element method, the meshless approximations for point distributions with high aspect ratios are typically of poor accuracy.

In this paper, we propose several approximation schemes to address the difficulties mentioned above—first, we propose a modification to the fixed kernel approximation to obtain the Kronecker delta property of the shape function; Second, we propose two approaches to satisfy the boundary conditions and the governing equations simultaneously at the boundary; and Third, for high aspect ratio elasticity problems, we propose an approach where the fixed kernel approximation reproduces the finite element stencil with reduced-order integration.

The key idea in a point collocation approach is to satisfy the governing partial differential equation(s) at each of the points covering the domain of interest. Point collocation is probably the simplest and the easiest approach to discretize the governing partial differential equations. The point collocation technique also has the advantage that it enforces the boundary conditions (Dirichlet, Neumann and mixed type) exactly. [1,7–10] have reported satisfactory results on solving various kinds of problems in mechanics using a collocation technique. Although a collocation technique gives satisfactory results for a large class of problems, when the point distribution is highly scattered and the solution is not smooth, the numerical results can be sensitive to the point distribution and the cloud size (or the support size). Oñate et al. [7,8,11] have observed some stability issues when applying the point collocation method to fluid flow problem. Benito et al. [12] also reported that the solution of the generalized finite difference method depends on the number of nodes in the cloud, the relative coordinates of the nodes with respect to the star node, and on the weighting function employed. It has been shown that the quality of a cloud can be controlled by satisfying the positivity conditions [13]. However, for a given set of scattered points in 2-D, the positivity conditions can often be violated, and one needs to modify the point distribution in the cloud to satisfy the positivity conditions. The stability of the meshless collocation methods can also be improved by employing more sophisticated collocation schemes instead of the simple point collocation technique. In this paper, we explore several collocation schemes and compare the performance of the various collocation schemes by using examples from 2-D elasticity and potential theory.

The rest of the paper is organized as follows: Section 2 presents a brief description of the fixed kernel approximation and several proposed improvements, Section 3 describes four kinds of collocation schemes, Section 4 compares the performance of the various collocation schemes by using 2-D potential and elastostatic problems as examples and finally, conclusions are given in Section 5.

2. Improvements to the fixed kernel approximation

2.1. Classical fixed kernel approximation

In the following, we outline the steps used for the construction of fixed kernel shape functions (see [1,6] for more details). The domain Ω is first represented by a set of NP points (or nodes), as shown in Fig. 1 for 2-dimensions. Then, for each node an approximation function is generated by constructing a cloud about that node (also referred to as a star node). A support/cloud is constructed by centering a kernel (i.e., the weighting function) about the star point. The kernel is non-zero at the star point and at few other nodes that are in the vicinity of the star point. The shape of the cloud, which defines the region at which the kernel is non-zero, can be

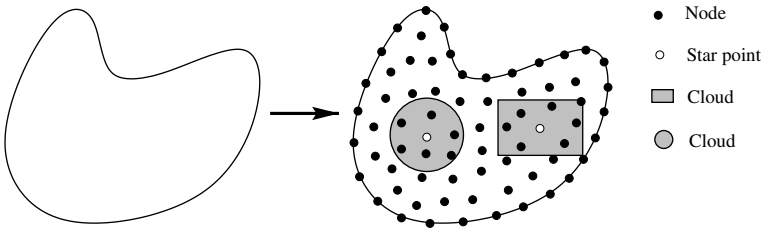

Fig. 1. Physical domain (left) is represented by a set of points (right). Clouds are constructed for each point. Also shown in the figure are circular and rectangular clouds.

arbitrary. Typical shapes we have employed are circles and rectangles in 2-D. In a fixed kernel approach, an approximation $u^a(x,y)$ to an unknown $u(x,y)$ is given by

$$u^a(x,y) = \int_\Omega \mathscr{C}(x,y,x_K-s,y_K-t)\phi(x_K-s,y_K-t) \times u(s,t)\mathrm{d}s\,\mathrm{d}t \tag{1}$$

where $\phi(x_K-s,y_K-t)$ is the kernel function centered at (x_K,y_K) and $\mathscr{C}(x,y,x_K-s,y_K-t)$ is the correction function which is given by

$$\mathscr{C}(x,y,x_K-s,y_K-t) = \mathbf{p}^{\mathrm{T}}(x_K-s,y_K-t)\mathbf{c}(x,y) \tag{2}$$

where $\mathbf{p}^{\mathrm{T}}(x_K-s,y_K-t) = \{p_1,p_2,\ldots,p_m\}$ is the $1\times m$ vector of basis functions and $\mathbf{c}^{\mathrm{T}}(x,y) = \{c_1,c_2,\ldots,c_m\}$ is the $1\times m$ vector of correction function coefficients. A quadratic basis is given by

$$\mathbf{p}^{\mathrm{T}}(x_K-s,y_K-t) = \left\{1,x_K-s,y_K-t,(x_K-s)^2,(x_K-s)(y_K-t),(y_K-t)^2\right\}, \quad m=6 \tag{3}$$

The unknown correction function coefficients can be determined by satisfying the reproducing or the consistency conditions, which are given by,

$$\int_\Omega \mathbf{p}^{\mathrm{T}}(x_K-s,y_K-t)\mathbf{c}(x,y)\phi(x_K-s,y_K-t)p_i(s,t)\mathrm{d}s\,\mathrm{d}t = p_i(x,y), \quad i=1,2,\ldots,m \tag{4}$$

A discrete approximation of the above consistency conditions is written as

$$\sum_{I=1}^{\mathrm{NP}} \mathbf{p}^{\mathrm{T}}(x_K-x_I,y_K-y_I)\mathbf{c}(x,y)\phi(x_K-x_I,y_K-y_I)p_i(x_I,y_I)\Delta V_I = p_i(x,y), \quad i=1,2,\ldots,m \tag{5}$$

where NP is the total number of points covering the domain Ω, and ΔV_I is the nodal volume associated with node I. The consistency conditions summarized in Eq. (5) can be written in a matrix form as

$$\mathbf{M}\mathbf{c}(x,y) = \mathbf{p}(x,y) \tag{6}$$

where $\mathbf{M}$ is the $m\times m$ moment matrix. The entries in the moment matrix are given by

$$\mathbf{M}_{ij} = \sum_{I=1}^{\mathrm{NP}} p_j(x_K-x_I,y_K-y_I) \times \phi(x_K-x_I,y_K-y_I)p_i(x_I,y_I)\Delta V_I \tag{7}$$

Note that for a given star point (x_K,y_K), $\mathbf{M}$ is a constant matrix, i.e., it is not a function of x and y. From Eq. (6), the unknown correction function coefficients are computed as

$$\mathbf{c}(x,y) = \mathbf{M}^{-1}\mathbf{p}(x,y) \tag{8}$$

Substituting the correction function coefficients into Eq. (1), we obtain

$$u^a(x,y) = \int_\Omega \mathbf{p}^{\mathrm{T}}(x,y)\mathbf{M}^{-\mathrm{T}}\mathbf{p}(x_K-s,y_K-t) \times \phi(x_K-s,y_K-t)u(s,t)\mathrm{d}s\,\mathrm{d}t \tag{9}$$

The approximation in Eq. (9) can be rewritten as

$$u^a(x,y) = \sum_{I=1}^{\mathrm{NP}} N_I(x,y)\hat{u}_I \tag{10}$$

where $\hat{u}_I$ is the unknown nodal parameter for node I, and $N_I(x,y)$ is the fixed kernel shape function (or approximation function) given by

$$N_I(x,y) = \mathbf{p}^{\mathrm{T}}(x,y)\mathbf{M}^{-\mathrm{T}}\mathbf{p}(x_K-x_I,y_K-y_I) \times \phi(x_K-x_I,y_K-y_I)\Delta V_I \tag{11}$$

Since the moment matrix (Eq. (7)) is constant, the derivatives of the shape function can be computed simply by differentiating the polynomial basis vector in Eq. (11). For example, the first and second x-derivatives are computed as:

$$N_{I,x}(x,y) = [\,0\quad 1\quad 0\quad 2x\quad y\quad 0\,]\mathbf{M}^{-\mathrm{T}} \times \mathbf{p}(x_K-x_I,y_K-y_I)\phi(x_K-x_I,y_K-y_I)\Delta V_I \tag{12}$$

$$N_{I,xx}(x,y) = [\,0\quad 0\quad 0\quad 2\quad 0\quad 0\,]\mathbf{M}^{-\mathrm{T}} \times \mathbf{p}(x_K-x_I,y_K-y_I)\phi(x_K-x_I,y_K-y_I)\Delta V_I \tag{13}$$

Note that one can choose (x_K,y_K) arbitrarily and consequently the shape function and its derivatives given in

Eq. (11)–(13) can be multivalued. A unique set of shape functions can be constructed by fixing (x_K, y_K) at the point (x, y), i.e., when computing $N_I(x, y)$, $I = 1,2,\ldots,NP$ and its derivatives, the center of the kernel function is fixed at (x, y) (see [1] for more details).

2.2. Kronecker delta property of the shape function

One drawback with both least-squares and kernel approximations is that the shape function does not satisfy the Kronecker delta property. As discussed in Section 1, this can impose difficulties in both collocation and weak form based meshless methods [13,14]. Various techniques [15–18] have been proposed in the literature to overcome this difficulty. These techniques have relied on a background grid structure [15,16], special form of the weighting function [17] or a significant change in the construction of the approximation [18]. In this section, we propose a simple modification to the fixed kernel approximation to enforce the Kronecker delta property. For a given cloud and its star point (x_K, y_K), we rewrite the fixed kernel approximation to the unknown $u(x, y)$ (Eq. (1)) as

$$u^a(x,y) = \sum_{I=1}^{NP} N_I(x,y)u(x_I,y_I) \tag{16}$$

$$N_I(x_J,y_J) = \begin{cases} 1 & J = I \\ 0 & J \neq I \end{cases} \tag{17}$$

It follows immediately from Eq. (14) that the zeroth-order consistency condition is satisfied. In the fixed kernel approximation, the uniqueness of the approximation function can be ensured by fixing the star point (x_K, y_K) at the point (x, y) (see [1] for more details). Denoting $x_K - x_I$ and $y_K - y_I$ as Δx_I and Δy_I, respectively, the first- and second-order consistency conditions can be written in a matrix form as

$$\begin{pmatrix} \sum \phi_I \Delta x_I^2 & \sum \phi_I \Delta x_I \Delta y_I & \sum \phi_I \Delta x_I^3 & \sum \phi_I \Delta x_I^2 \Delta y_I & \sum \phi_I \Delta x_I \Delta y_I^2 \\ \sum \phi_I \Delta x_I \Delta y_I & \sum \phi_I \Delta y_I^2 & \sum \phi_I \Delta x_I^2 \Delta y_I & \sum \phi_I \Delta x_I \Delta y_I^2 & \sum \phi_I \Delta y_I^3 \\ \sum \phi_I \Delta x_I^3 & \sum \phi_I \Delta x_I^2 \Delta y_I & \sum \phi_I \Delta x_I^4 & \sum \phi_I \Delta x_I^3 \Delta y_I & \sum \phi_I \Delta x_I^2 \Delta y_I^2 \\ \sum \phi_I \Delta x_I^2 \Delta y_I & \sum \phi_I \Delta x_I \Delta y_I^2 & \sum \phi_I \Delta x_I^3 \Delta y_I & \sum \phi_I \Delta x_I^2 \Delta y_I^2 & \sum \phi_I \Delta x_I \Delta y_I^3 \\ \sum \phi_I \Delta x_I \Delta y_I^2 & \sum \phi_I \Delta y_I^3 & \sum \phi_I \Delta x_I^2 \Delta y_I^2 & \sum \phi_I \Delta x_I \Delta y_I^3 & \sum \phi_I \Delta y_I^4 \end{pmatrix} \begin{Bmatrix} c_1 \\ c_2 \\ c_3 \\ c_4 \\ c_5 \end{Bmatrix} = \begin{Bmatrix} (x-x_K) \\ (y-y_K) \\ (x-x_K)^2 \\ (x-x_K)(y-y_K) \\ (y-y_K)^2 \end{Bmatrix}_{x=x_K, y=y_K} = \begin{Bmatrix} 0 \\ 0 \\ 0 \\ 0 \\ 0 \end{Bmatrix} \tag{18}$$

$$u^a(x,y) - u(x_K,y_K) = \int_\Omega \mathscr{C}(x,y,x_K-s,y_K-t) \times \phi(x_K-s,y_K-t) \times [u(s,t)-u(x_K,y_K)]\,ds\,dt \tag{14}$$

In the following, we show that if the correction function $\mathscr{C}(x, y, x_K - s, y_K - t)$ is of the form

$$\mathscr{C} = c_1(x_K-s) + c_2(y_K-t) + c_3(x_K-s)^2 + c_4(x_K-s)(y_K-t) + c_5(y_K-t)^2 \tag{15}$$

and the consistency conditions up to the second order are imposed, the fixed kernel approximation satisfies the Kronecker delta property, i.e.,

Assuming the weighting function is $\phi \in C^0$ and the point distributions are regular [13], the moment matrix in Eq. (18) is non-singular. Therefore, from Eq. (18),

$$c_1 = c_2 = c_3 = c_4 = c_5 = 0 \tag{19}$$

Eq. (14) can be written in a discrete form as

$$u^a(x,y) - u(x_K,y_K) = \sum_{I=1}^{NP} \mathscr{C}(x,y,x_K-x_I,y_K-y_I)\phi(x_K - x_I, y_K - y_I)[u(x_I,y_I) - u(x_K,y_K)]\Delta V_I \tag{20}$$

Since the approximation is constructed by fixing (x_K, y_K) at the point (x, y), Eq. (20) can be rewritten in short form as

$$\begin{aligned} u^a(x,y)|_{x=x_K,y=y_K} &= \sum_{I=1,I\neq K}^{NP} N_I(x_K,y_K)u(x_I,y_I) - u(x_K,y_K)\sum_{I=1,I\neq K}^{NP} N_I(x_K,y_K) + u(x_K,y_K) \\ &= \sum_{I=1}^{NP} N_I(x_K,y_K)u(x_I,y_I) \end{aligned} \tag{21}$$

where

$$N_I(x_K,y_K)=\begin{cases}\mathscr{C}(x_K,y_K,x_K-x_I,y_K-y_I)\\ \quad\times\phi(x_K-x_I,y_K-y_I)\Delta V_I\\ \quad I\neq K\\ 1-\sum\limits_{I=1,I\neq K}^{\mathrm{NP}}\mathscr{C}(x_K,y_K,x_K-x_I,\\ \quad y_K-y_I)\phi(x_K-x_I,y_K-y_I)\Delta V_I\\ \quad I=K\end{cases}\tag{22}$$

Substituting Eq. (19) into Eq. (15), it follows that $\mathscr{C}(x_K,y_K,x_K-x_I,y_K-y_I)=0$. Therefore

$$N_I(x_K,y_K)=\begin{cases}0 & I\neq K\\ 1 & I=K\end{cases}\tag{23}$$

2.3. Approximations at the boundary nodes

Typically, in the point collocation technique, either the governing equation or the boundary condition is enforced for a boundary point. It is difficult to satisfy both the governing equation and the boundary condition at the same point since the number of unknowns at a point must equal the number of equations. In this section, we propose two approaches to satisfy both the boundary condition and the governing equation at the boundary points.

2.3.1. Enforcing the boundary conditions in the construction of the shape functions

We refer to the first approach as the embedding boundary condition technique. The key idea in this technique is to enforce the boundary condition into the approximation of the boundary point and then to satisfy the governing equation in the collocation discretization. The approach is described using the classical fixed kernel approximation. The extension of the approach to the least-squares and other approximations is straight-forward. Assuming the unknown u at a boundary point (x,y) is approximated by a general polynomial

$$u^a(x,y)=c_0+c_1x+c_2y+c_3x^2+\cdots\tag{24}$$

or

$$u^a(x,y)=\mathbf{p}^{\mathrm{T}}\mathbf{c}\quad c\in\{c_0,c_1,\ldots,c_{m-1}\}\tag{25}$$

where $\mathbf{p}^{\mathrm{T}}=\{1\ x\ y\ x^2\ \ldots\}$ is the polynomial basis and $\mathbf{c}$ is the unknown coefficient vector. Assume that there are q boundary conditions specified on the boundary point (x,y), which are given by

$$\mathscr{B}_i(u^a(x,y))=f_i(x,y)\quad i=1,2,\ldots,q\quad\text{and}\quad q\leqslant m\tag{26}$$

Substituting Eq. (24) into Eqs. (26), Eq. (26) can be rewritten in a matrix form

$$\mathbf{B}_{q\times m}\mathbf{c}_{m\times1}=\mathbf{f}_{q\times1}\tag{27}$$

Eq. (27) is typically a rectangular linear system which can be further written as

$$\left[\mathbf{B1}_{q\times q}\mathbf{B2}_{q\times(m-q)}\right]\begin{Bmatrix}c_0\\ c_1\\ \vdots\\ c_{q-1}\\ c_q\\ \vdots\\ c_{m-1}\end{Bmatrix}=\mathbf{f}_{q\times1}\tag{28}$$

For illustration purpose, we assume **B1** in Eq. (28) is non-singular. In practice, one may need to perform pivoting on Eq. (28) to ensure that **B1** is non-singular. Defining $\hat{\mathbf{c}}^{\mathrm{T}}=\{c_0\ c_1\ \cdots\ c_{q-1}\}$ and $\bar{\mathbf{c}}^{\mathrm{T}}=\{c_q\ c_{q+1}\ \cdots\ c_{m-1}\}$, Eq. (28) can be rewritten as

$$\mathbf{B1}_{q\times q}\hat{\mathbf{c}}_{q\times1}+\mathbf{B2}_{q\times(m-q)}\bar{\mathbf{c}}_{(m-q)\times1}=\mathbf{f}_{q\times1}\tag{29}$$

Therefore,

$$\begin{aligned}\hat{\mathbf{c}}_{q\times1}&=-\mathbf{B1}^{-1}_{q\times q}\mathbf{B2}_{q\times(m-q)}\bar{\mathbf{c}}_{(m-q)\times1}+\mathbf{B1}^{-1}_{q\times q}\mathbf{f}_{q\times1}\\&=\mathbf{R}_{q\times(m-q)}\bar{\mathbf{c}}_{(m-q)\times1}+\mathbf{f}'_{q\times1}\end{aligned}\tag{30}$$

where $\mathbf{R}=-\mathbf{B1}^{-1}\mathbf{B2}$ and $\mathbf{f}'=\mathbf{B1}^{-1}\mathbf{f}$. By using the definition of $\hat{\mathbf{c}}$ and $\bar{\mathbf{c}}$, Eq. (25) can be rewritten as

$$u^a(x,y)=\mathbf{p}_1^{\mathrm{T}}\hat{\mathbf{c}}+\mathbf{p}_2^{\mathrm{T}}\bar{\mathbf{c}}\tag{31}$$

where $\mathbf{p}_1$ and $\mathbf{p}_2$ are the basis functions corresponding to the coefficients $\hat{\mathbf{c}}$ and $\bar{\mathbf{c}}$. Substituting Eq. (30) into Eq. (31), the approximation of the unknown u can be rewritten as

$$u^a(x,y)=p_0(x,y)+\bar{\mathbf{p}}^{\mathrm{T}}(x,y)\bar{\mathbf{c}}\tag{32}$$

where $p_0(x,y)=\mathbf{p}_1^{\mathrm{T}}\mathbf{f}'$, $\bar{\mathbf{p}}^{\mathrm{T}}(x,y)=\mathbf{p}_1^{\mathrm{T}}\mathbf{R}+\mathbf{p}_2^{\mathrm{T}}$ and $\bar{\mathbf{c}}$ is the remaining unknown coefficients to be determined. The boundary conditions (Eq. (26)) are hence embedded into the new approximation of the unknown (Eq. (32)). Taking $\bar{\mathbf{p}}^{\mathrm{T}}(x,y)$ as the basis functions, the remaining independent unknown coefficients $\bar{\mathbf{c}}$ can then be determined by using the fixed kernel approximation. The approximation is written as

$$\begin{aligned}u^a(x,y)-p_0(x,y)=\int_\Omega&\bar{\mathbf{p}}^{\mathrm{T}}(s,t)\bar{\mathbf{c}}(x,y)\phi(x_K-s,y_K-t)\\&\times[u(s,t)-p_0(s,t)]\mathrm{d}s\,\mathrm{d}t\end{aligned}\tag{33}$$

The consistency conditions for $\bar{\mathbf{p}}(x,y)$ gives

$$\begin{aligned}\bar{\mathbf{p}}(x,y)=&\int_\Omega\bar{\mathbf{p}}^{\mathrm{T}}(s,t)\bar{\mathbf{c}}(x,y)\phi(x_K-s,y_K-t)\bar{\mathbf{p}}(s,t)\mathrm{d}s\,\mathrm{d}t\\&j=1,2,\ldots,m-q\end{aligned}\tag{34}$$

In a matrix form, the consistency conditions can be written as

$$\overline{\mathbf{M}}\bar{\mathbf{c}}(x,y)=\bar{\mathbf{p}}(x,y)\tag{35}$$

where

$$\overline{\mathbf{M}}_{ij} = \sum_{I=1}^{\mathrm{NP}} \overline{p}_j(x_I, y_I)\phi(x_K - x_I, y_K - y_I)\overline{p}_i(x_I, y_I)\Delta V_I \quad (36)$$

Thus, $\overline{\mathbf{c}}$ can be computed by

$$\overline{\mathbf{c}}(x, y) = \overline{\mathbf{M}}^{-1}\overline{\mathbf{p}}(x, y) \quad (37)$$

Substituting Eq. (37) into Eq. (33), the discrete form of the approximation of the unknown u and its derivatives can be written as

$$u^a(x, y) = p_0(x, y) + \sum_{I=1}^{\mathrm{NP}} \overline{N}_I(x, y)\hat{u}_I - \sum\nolimits_{I=1}^{\mathrm{NP}} \overline{N}_I(x, y)p_0(x_I, y_I) \quad (38)$$

$$\frac{\partial u^a(x, y)}{\partial x} = \frac{\partial p_0(x, y)}{\partial x} + \sum_{I=1}^{\mathrm{NP}} \frac{\partial \overline{N}_I(x, y)}{\partial x}\hat{u}_I - \sum_{I=1}^{\mathrm{NP}} \frac{\partial \overline{N}_I(x, y)}{\partial x}p_0(x_I, y_I) \quad (39)$$

$$\frac{\partial^2 u^a(x, y)}{\partial x^2} = \frac{\partial^2 p_0(x, y)}{\partial x^2} + \sum_{I=1}^{\mathrm{NP}} \frac{\partial^2 \overline{N}_I(x, y)}{\partial x^2}\hat{u}_I - \sum_{I=1}^{\mathrm{NP}} \frac{\partial^2 \overline{N}_I(x, y)}{\partial x^2}p_0(x_I, y_I) \quad (40)$$

where

$$\overline{N}_I(x, y) = \overline{\mathbf{p}}^{\mathrm{T}}(x, y)\overline{\mathbf{M}}^{-\mathrm{T}}\overline{\mathbf{p}}(x_I, y_I)\phi(x_K - x_I, y_K - y_I)\Delta V_I \quad (41)$$

2.3.2. Hermite-type fixed kernel approximation for the boundary nodes

Another approach to satisfy both the governing equation and the boundary condition is to include more independent variables for the boundary nodes. Hermite-type interpolation and approximation schemes [9,19,20] treat the normal derivative of the unknown as an independent variable. In this section, we introduce a Hermite-type fixed kernel approximation for the boundary nodes, i.e.,

$$u^a = \int_\Omega \mathbf{p}^{\mathrm{T}}(s, t)\tilde{\mathbf{c}}(x, y)\phi(x_K - s, y_K - t)u(s, t)\,\mathrm{d}s\,\mathrm{d}t + \alpha\int_\Gamma \frac{\partial \mathbf{p}^{\mathrm{T}}}{\partial n}(s, t)\tilde{\mathbf{c}}(x, y)\phi(x_K - s, y_K - t)q(s, t)\,\mathrm{d}s\,\mathrm{d}t \quad (42)$$

where Γ is the boundary of the domain, n is the boundary outward normal, α is a constant accounting for dimensionality analysis (typically $\alpha = 1$ is used for convenience), $\mathbf{p}$ is the base interpolating polynomial, $\tilde{\mathbf{c}}$ is the unknown correction function coefficient vector and $q(x, y)$ is the normal derivative of the unknown $u(x, y)$.

The correction function coefficients can be determined by applying the consistency conditions. A discrete approximation of the consistency conditions is written as

$$p_i(x, y) = \sum_{I=1}^{\mathrm{NP}} \mathbf{p}^{\mathrm{T}}(x_I, y_I)\tilde{\mathbf{c}}(x, y)\phi(x_K - x_I, y_K - y_I) \times p_i(x_I, y_I)\Delta V_I + \sum_{I=1}^{\mathrm{NB}} \frac{\partial \mathbf{p}^{\mathrm{T}}}{\partial n}(x_I, y_I) \times \tilde{\mathbf{c}}(x, y)\phi(x_K - x_I, y_K - y_I) \times \frac{\partial p_i}{\partial n}(x_I, y_I)\Delta V_I \quad i = 1, 2, \ldots, m \quad (43)$$

where NB is the number of boundary points. Eq. (43) can rewritten in a matrix form as

$$\tilde{\mathbf{M}}\tilde{\mathbf{c}}(x, y) = \mathbf{p}(x, y) \quad (44)$$

where the entries of the moment matrix $\tilde{\mathbf{M}}$ are given by

$$\tilde{\mathbf{M}}_{ij} = \sum_{I=1}^{\mathrm{NP}} p_j(x_I, y_I)\phi(x_K - x_I, y_K - y_I)p_i(x_I, y_I)\Delta V_I \quad (45)$$

$$+ \sum_{I=1}^{\mathrm{NB}} \frac{\partial p_j}{\partial n}(x_I, y_I)\phi(x_K - x_I, y_K - y_I)\frac{\partial p_i}{\partial n}(x_I, y_I)\Delta V_I \quad (46)$$

The unknown correction function coefficients are computed by

$$\tilde{\mathbf{c}}(x, y) = \tilde{\mathbf{M}}^{-1}\mathbf{p}(x, y) \quad (47)$$

Substituting Eq. (47) into Eq. (42), the Hermite-type fixed kernel approximation can be written in the discrete form as

$$u^a = \mathbf{p}^{\mathrm{T}}(x, y)\tilde{\mathbf{M}}^{-\mathrm{T}}\sum_{I=1}^{\mathrm{NP}} \mathbf{p}(x_I, y_I)\phi(x_K - x_I, y_K - y_I)\Delta V_I\hat{u}_I + \mathbf{p}^{\mathrm{T}}(x, y)\tilde{\mathbf{M}}^{-\mathrm{T}}\sum_{I=1}^{\mathrm{NB}} \frac{\partial \mathbf{p}(x_I, y_I)}{\partial n}\phi(x_K - x_I, y_K - y_I)\Delta V_I\hat{q}_I \quad (48)$$

and the first and second x derivatives, for example, are computed as

$$\frac{\partial u^a}{\partial x} = \frac{\partial \mathbf{p}^{\mathrm{T}}(x, y)}{\partial x}\tilde{\mathbf{M}}^{-\mathrm{T}}\sum_{I=1}^{\mathrm{NP}} \mathbf{p}(x_I, y_I)\phi(x_K - x_I, y_K - y_I)\Delta V_I\hat{u}_I + \frac{\partial \mathbf{p}^{\mathrm{T}}(x, y)}{\partial x}\tilde{\mathbf{M}}^{-\mathrm{T}}\sum_{I=1}^{\mathrm{NB}} \frac{\partial \mathbf{p}(x_I, y_I)}{\partial n}\phi(x_K - x_I, y_K - y_I)\Delta V_I\hat{q}_I \quad (49)$$

$$\frac{\partial^2 u^a}{\partial x^2} = \frac{\partial^2 \mathbf{p}^{\mathrm{T}}(x, y)}{\partial x^2}\tilde{\mathbf{M}}^{-\mathrm{T}}\sum\nolimits_{I=1}^{\mathrm{NP}} \mathbf{p}(x_I, y_I)\phi(x_K - x_I, y_K - y_I)\Delta V_I\hat{u}_I + \frac{\partial^2 \mathbf{p}^{\mathrm{T}}(x, y)}{\partial x^2}\tilde{\mathbf{M}}^{-\mathrm{T}}\sum\nolimits_{I=1}^{\mathrm{NB}} \frac{\partial \mathbf{p}(x_I, y_I)}{\partial n}\phi(x_K - x_I, y_K - y_I) \times \Delta V_I\hat{q}_I \quad (50)$$

Remarks

- The embedding boundary condition technique enforces multiple boundary conditions at the boundary nodes without adding additional degrees of freedom. The number of the unknowns remains the same, and the computational cost to solve the final linear system does not increase.
- Compared to the construction of the Hermite-type fixed kernel shape functions, the construction of the shape functions using the embedding boundary condition approach is more complicated and expensive, since an additional under-determined system needs to be solved for each boundary point. In addition, we observe that the Hermite-type shape functions typically provide higher accuracy compared to the shape functions obtained by the embedding boundary condition approach. Therefore, we adopt the Hermite-type approximation for the boundary nodes in this paper.
- The Hermite-type approximation and the embedding boundary condition approach can also be used with the moving kernel, the fixed least-squares and the moving least-squares approximations.

2.4. Approximation functions for high aspect ratio problems

In many engineering applications, structures with a high aspect ratio are often encountered. In such structures, if points are distributed evenly over the domain, a large number of points are required to cover the structural domain. It is desirable to reduce the number of points, especially along the dimension with a larger length, so that the point distribution is not uniform. Unfortunately, like other conventional methods, when a high aspect ratio structure, such as a thin beam, is subjected to bending, the solution with the finite cloud method deteriorates as the aspect ratio of the point distribution increases. This phenomena is called "shear locking" in the finite element method. In this section, we investigate possible approaches to improve the performance of FCM with high aspect ratio point distributions.

2.4.1. High order basis functions

It is well-known that for beam bending problems, the shear strain is quite small. In the expression for the shear strain

$$\gamma_{xy} = \frac{\partial u}{\partial y} + \frac{\partial v}{\partial x} \tag{51}$$

the two terms on the right hand side have relatively large values, compared to the shear strain, with opposite signs. In the FCM, $\partial u/\partial y$ and $\partial v/\partial x$ are approximated by using the fixed kernel approximation. When the distance between the points in, e.g., the x-direction is much larger than in the y-direction, the truncation error of the approximation in the x-direction is much higher than the truncation error in the y-direction. Since $\partial u/\partial y$ and $\partial v/\partial x$ cancel with each other, the truncation error is largely magnified. Therefore, one approach to overcome this problem is to increase the accuracy of the approximation to reduce the truncation error of $\partial u/\partial y$ and $\partial v/\partial x$.

To reduce the truncation error of the approximation, one can utilize a high-order basis. For example, a sixth-order basis in 2-D

$$\mathbf{p}(s,t) = \begin{bmatrix} 1 & s & t & s^2 & st & t^2 & s^3 & s^2t & st^2 & t^3 \\ s^4 & s^3t & s^2t^2 & st^3 & t^4 & s^5 & s^4t & s^3t^2 & s^2t^3 & st^4 \\ t^5 & s^6 & s^5t & s^4t^2 & s^3t^3 & s^2t^4 & st^5 & t^6 & & \end{bmatrix} \tag{52}$$

gives accurate results for a point distribution with an aspect ratio of up to 15:1.

Remarks

- When high-order basis functions are used, the cloud size for a point is typically large, and the dimension of the moment matrix also increases. For the sixth-order basis functions given above, the moment matrix is 28×28. Hence, the cost of computing the shape function or the approximation function for a point increases even though the total number of points decreases.
- The high-order basis approach can reduce the truncation error when a rectangular point distribution is used. For scattered point distributions with a high aspect ratio, the cloud could be ill-balanced and the positivity conditions can be easily violated (see [13]). For this reason, the high-order basis approach is not effective for scattered point distributions. Therefore, the high-order basis approach is of limited use in practice and a more efficient approach is desirable.

2.4.2. FEM reduced integration stencil

In the finite element method, a weak form of the governing equations is first generated based on a variational approach, and integrations are then performed on each element to generate the element stiffness matrices which are assembled into the global stiffness matrix. In the finite cloud method, a collocation approach directly

assembles the shape functions and their derivatives at each point into the row of the global matrix corresponding to that point. Even though these two methods are somewhat different mathematically, it can be shown that, for a given finite element mesh with rectangular elements, one can simply take the finite element nodes as the meshless points and use the finite cloud method to generate an equivalent final linear system and obtain an identical solution to the FEM solution by choosing proper weightings for the points in the cloud.

In the following, we take the simple potential problem, $\nabla^2 u(x,y) = 0$, to illustrate the approach. Fig. 2 shows a cluster of four rectangular quadrilateral finite elements centered at (0,0). Each element has a length Δx and width Δy. The standard element stiffness matrix for element 1 can be written as

$$\mathbf{k}_1 = \begin{bmatrix} k_{11} & k_{12} & k_{13} & k_{14} \\ k_{21} & k_{22} & k_{23} & k_{24} \\ k_{31} & k_{32} & k_{33} & k_{34} \\ k_{41} & k_{42} & k_{43} & k_{44} \end{bmatrix} \tag{53}$$

where

$$k_{ij} = k_{ji} = \int_{V1} (N^{\text{fem}}_{i,x} N^{\text{fem}}_{j,x} + N^{\text{fem}}_{i,y} N^{\text{fem}}_{j,y}) dV_1 \quad i,j = 1,2,3,4 \tag{54}$$

and $V1$ denotes the area of element 1. For illustration purpose, the isoparametric mapping is not used here. The finite element shape functions can be directly written as

$$N^{\text{fem}}_1 = \left(1 - \frac{x}{\Delta x}\right)\left(1 - \frac{y}{\Delta y}\right) \tag{55}$$

$$N^{\text{fem}}_2 = \frac{x}{\Delta x}\left(1 - \frac{y}{\Delta y}\right) \tag{56}$$

$$N^{\text{fem}}_3 = \frac{x}{\Delta x}\frac{y}{\Delta y} \tag{57}$$

$$N^{\text{fem}}_4 = \left(1 - \frac{x}{\Delta x}\right)\frac{y}{\Delta y} \tag{58}$$

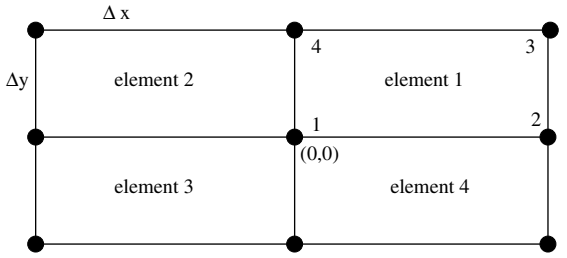

Fig. 2. Rectangular finite element configuration for a point at (0,0).

When a full numerical integration scheme is used, the integrations in Eq. (54) are evaluated exactly. For example

$$\int_{V1} (N^{\text{fem}}_{1,x} N^{\text{fem}}_{1,x}) dV_1 = \int_{V1} \left[\left(\frac{1}{\Delta x}\right)\left(1 - \frac{y}{\Delta y}\right)\right]^2 \mathrm{d}x\,\mathrm{d}y = \frac{1}{3}\frac{\Delta y}{\Delta x} \tag{59}$$

Similarly

$$\int_{V1} (N^{\text{fem}}_{1,x} N^{\text{fem}}_{2,x}) \mathrm{d}V_1 = -\frac{1}{3}\frac{\Delta y}{\Delta x} \tag{60}$$

$$\int_{V1} (N^{\text{fem}}_{1,x} N^{\text{fem}}_{3,x}) \mathrm{d}V_1 = -\frac{1}{6}\frac{\Delta y}{\Delta x} \tag{61}$$

$$\int_{V1} (N^{\text{fem}}_{1,x} N^{\text{fem}}_{4,x}) \mathrm{d}V_1 = \frac{1}{6}\frac{\Delta y}{\Delta x} \tag{62}$$

Therefore, all the entries of matrix $\mathbf{k}_1$ can be computed. Note that when the matrix $\mathbf{k}_1$ is assembled into the global stiffness matrix, the entries are added according to their local-global node index mapping. After all the four elements in Fig. 2 are integrated and assembled into the global stiffness matrix, the row in the global matrix for point (0,0) is fully determined. The values of the entries in that row determine the FEM stencil for point (0,0). In Eq. (54), there are two terms in each integration: the x-derivative term and the y-derivative term. These two terms in the weak form correspond to the $\partial^2 u/\partial x^2$ and $\partial^2 u/\partial y^2$ terms in the governing equation, respectively. We compute the FEM stencil separately into an x-stencil and a y-stencil. The FEM stencils for the point (0,0) are shown in Fig. 3.

In the finite cloud method, the stencil of a point is assembled by collocating the governing equation at that point. For the potential equation, the second derivatives of the unknown $u(x,y)$ in the governing equation are approximated by using the second derivatives of the meshless shape function, i.e., $N_{,xx}$ and $N_{,yy}$ (N here, for example, is the shape function defined in Eq. (11)). Therefore, the effect of $N_{,xx}$ and $N_{,yy}$ resembles the effect of $\int N^{\text{fem}}_{,x} N^{\text{fem}}_{,x} \mathrm{d}x\,\mathrm{d}y$ and $\int N^{\text{fem}}_{,y} N^{\text{fem}}_{,y} \mathrm{d}x\,\mathrm{d}y$ in the finite element method. For the center point (0,0), one can set up a cloud centered at point (0,0) and cover the nine points shown in Fig. 2. If one uses the weighting scheme shown in Fig. 4 for the cloud, the resultant FCM stencils are as shown in Fig. 5. Comparing Fig. 5 with Fig. 3, it is easy to see that when the FCM stencils are multiplied by a constant $\Delta x \Delta y$ the FEM stencils and the FCM stencils are identical. Thus, for the rectangular quadrilateral elements, the FEM stencils can be reproduced within the framework of the finite cloud method if a proper weighting scheme is chosen. Since the "shear locking" phenomena can be reduced in FEM by using a reduced integration scheme for the shear strain, one can further manipulate the weights for the points in the cloud to

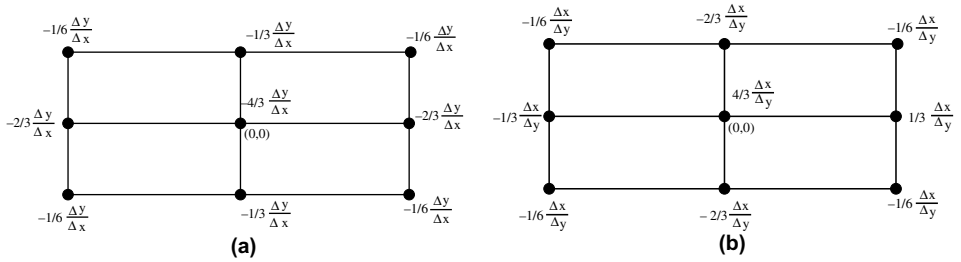

Fig. 3. FEM stencils for $\int N^{\text{fem}}_{,x} N^{\text{fem}}_{,x}\,\mathrm{d}x\,\mathrm{d}y$ (a) and $\int N^{\text{fem}}_{,y} N^{\text{fem}}_{,y}\,\mathrm{d}x\,\mathrm{d}y$ (b).

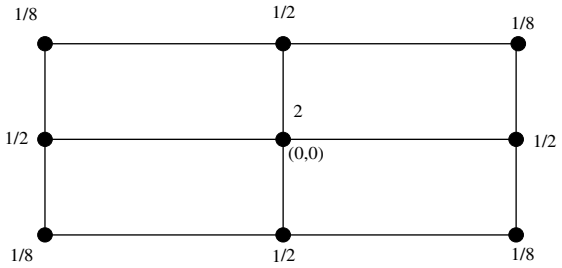

Fig. 4. FCM weighting to reproduce the FEM stencils.

reproduce the FEM reduced-order integration stencils. Derivation of the FCM stencil which reproduces the reduced integration FEM stencil for the elastostatic problem is given in Appendix A.

An example containing a high aspect ratio fixed-fixed elastic beam subjected to a uniform pressure is shown in Fig. 6. Fig. 7 shows the numerical results for the fixed-fixed beam shown in Fig. 6. The beam has a geometry of 20×1. The Young's modulus is $E = 1.69\text{e}{+3}$ and Poisson's ratio $v = 0.3$. The surface pressure is set to be 0.5. The results show that the FEM equivalent FCM scheme produces accurate results up to an aspect ratio of 8:1 for the point distribution.

Remarks

- The locking problem in meshless methods with a high aspect ratio point distribution can be reduced by using a higher order polynomial interpolation and/or by using a reduced-order integration. However, these approaches avoid the locking only in some cases. To avoid locking for structures with incompressible material (''volumetric locking''), displacement/pressure mixed interpolation/approximation techniques together with a reduced-order integration are typically employed in the finite element method [21]. The mixed approximation techniques have been empolyed in several weak form based meshless methods [22–24] to solve incompressible problems. The application of the mixed approximation techniques in collocation based meshless methods is still an open research topic.

3. Collocation schemes

In Section 2, we have proposed several approaches to improve the fixed kernel approximation. Taking advantage of these improvements (shape function with the Kronecker delta property and the Hermite-type approximation for the boundary nodes), we investigate the second major step of the finite cloud method: collocation

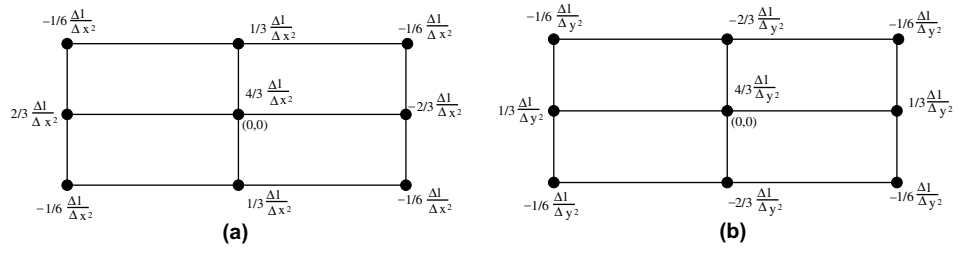

Fig. 5. FCM stencils for the second x-derivative of the meshless shape function $N_{,xx}$ (a) and the second y-derivative of the meshless shape function $N_{,yy}$ (b).

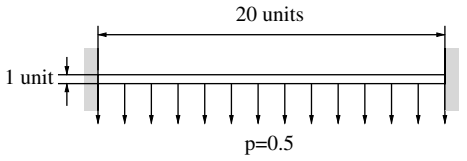

Fig. 6. A high aspect ratio fixed-fixed beam subjected to a uniform pressure. The length of the beam is 20 units and the thickness of the beam is 1 unit.

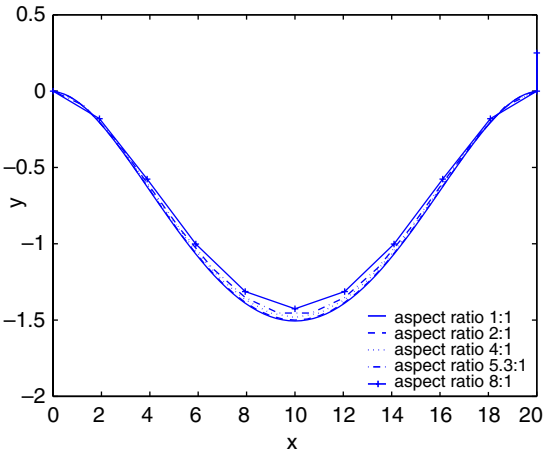

Fig. 7. FCM results for the fixed-fixed beam shown in Fig. 6 obtained by using the FEM-equivalent stencils.

discretization. Four types of collocation schemes for the governing equation are considered in this section: point collocation, strong form local domain collocation, local domain least-squares collocation and double grid collocation.

3.1. Point collocation

Point collocation is the simplest and the easiest way to discretize the governing equations. In a point collocation approach, the governing equations for a physical problem can be written in the following general form:

$$\mathscr{L}u(x,y) = f(x,y) \quad \text{in} \quad \Omega \tag{63}$$

$$\mathscr{G}u(x,y) = g(x,y) \quad \text{on} \quad \Gamma_g \tag{64}$$

$$\mathscr{H}u(x,y) = h(x,y) \quad \text{on} \quad \Gamma_h \tag{65}$$

where Ω is the domain, Γ_g is the portion of the boundary on which Dirichlet boundary conditions are specified, Γ_h is the portion of the boundary on which Neumann boundary conditions are specified and $\mathscr{L}$, $\mathscr{G}$ and $\mathscr{H}$ are the differential, Dirichlet and Neumann operators, respectively. The boundary of the domain is given by $\Gamma = \Gamma_g \cup \Gamma_h$. After the meshless shape functions are constructed, for each interior node, the point collocation technique simply substitutes the approximated unknown into the governing equations. In the classical point collocation aprpoach, for nodes with prescribed boundary conditions, the approximate solution or the derivative of the approximate solution are substituted into the given Dirichlet and Neumann-type boundary conditions, respectively. Therefore, the discretized governing equations are given by

$$\mathscr{L}u^a(x,y) = f(x,y) \quad \text{for points in} \quad \Omega \tag{66}$$

$$\mathscr{G}u^a(x,y) = g(x,y) \quad \text{for points on} \quad \Gamma_g \tag{67}$$

$$\mathscr{H}u^a(x,y) = h(x,y) \quad \text{for points on} \quad \Gamma_h \tag{68}$$

In the embedding boundary condition approach introduced in Section 2.3.1, the boundary conditions (Eqs. (64), (65)) are embedded into the shape functions and the governing equations are satisfied at all nodes, i.e.,

$$\mathscr{L}u^a(x,y) = f(x,y) \quad \text{for all points in } \Omega \quad \text{and on } \Gamma \tag{69}$$

In the Hermite-type approximation approach (Section 2.3.2), the normal derivative of the unknown at the boundary nodes is taken as an independent variable. Given a boundary node, the governing equation and the boundary condition are satisfied simultaneously. Therefore, the discretized governing equations are given by

$$\mathscr{L}u^a(x,y) = f(x,y) \quad \text{for all points in } \Omega \quad \text{and on } \Gamma \tag{70}$$

$$\mathscr{G}u^a(x,y) = g(x,y) \quad \text{for points on} \quad \Gamma_g \tag{71}$$

$$\mathscr{H}u^a(x,y) = h(x,y) \quad \text{for points on} \quad \Gamma_h \tag{72}$$

When the interpolating (Kronecker delta property) meshless shape functions are used, the point collocation approach gives rise to a linear system of equations of the form

$$\mathbf{Ku} = \mathbf{F} \tag{73}$$

The solution of Eq. (73) provides the solution at the nodes. Note that if the shape functions do not satisfy the Kronecker delta property, Eq. (73) would be $\mathbf{K}\hat{\mathbf{u}} = \mathbf{F}$, where $\hat{\mathbf{u}}$ are the nodal parameters and the solution $\mathbf{u}$ is computed by using Eq. (10).

Remarks

1. In this paper, the point collocation approach is implemented with the interpolating shape functions and their derivatives for the interior points and Hermite-type approximation for the boundary nodes.

2. We have found that, for scattered point distributions, the quality of the clouds can directly influence the numerical error in the solution. When the point distribution is highly scattered, it is likely that certain stability conditions, namely the positivity conditions (see [13] for details), could be violated for certain clouds. For this reason, the modified Gaussian, cubic or quartic inverse distance functions [13] are better choices for the kernel/weighting function in point collocation. In [13], we have proposed quantitative criteria to measure the cloud quality and approaches to ensure the satisfaction of the positivity conditions for 1-D and 2-D problems. However, for really bad point distributions, it could be difficult to satisfy the positivity conditions and modification of the point distribution may be necessary.

3.2. Strong form local domain collocation

For a scattered point distribution, the standard collocation can be sensitive to the point distribution in the clouds. When the point distribution is highly scattered, it is difficult to define a well balanced cloud. Instead of satisfying the governing equation at each node, the strong form local domain collocation (or subdomain collocation) [21] enforces the average residual in a local domain surrounding the star point to be zero, i.e.,

$$\int_{\Omega_s} w(x,y)(\mathscr{L}u(x,y) - f(x,y))\mathrm{d}\Omega = 0 \tag{74}$$

where Ω_s is the local integration domain of the star point (x,y) and $w(x,y)$ is the weighting function centered at the star point. One can chose various kinds of functions, e.g. constant, Gaussian or cubic spline functions, as the weighting function. In this paper, the weighting function $w(x,y)$ is taken as the kernel function given in Eq. (1),

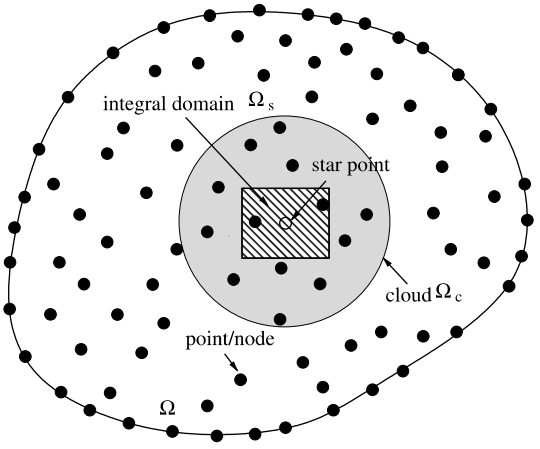

Fig. 8. Strong form local domain collocation.

which vanishes outside the cloud (denoted as Ω_c in Fig. 8). A typical cloud and the local integration domain of a star point are shown in Fig. 8. The circle is the cloud. The shaded rectangle is used as the local integration domain. Note that although the size and shape of the local integration domain can be arbitrary, we have observed that the results are more accurate when $\cup\Omega_s \approx \Omega$ and the integration domains of the points do not overlap too much. In this paper, square local integration domains are used and the minimum distance from the points to the star point is chosen as the width of the local integration domain. Typically, nine Gauss quadrature points are used in the local domain for integration purpose. The fixed kernel approximation is used to evaluate the derivatives at the Gauss quadrature points. For example, consider the Laplace equation

$$\nabla^2 u(x,y) = 0 \tag{75}$$

For a star point (x_I, y_I), the discretized form of Eq. (74) can be written as

$$\sum_{Q=1}^{\mathrm{NG}} w(x_Q^I, y_Q^I) W_g(x_Q^I, y_Q^I) \times \sum_{J=1}^{\mathrm{NP}} \left[\frac{\partial^2 \mathbf{N}_J}{\partial x^2}(x_Q^I, y_Q^I) + \frac{\partial^2 \mathbf{N}_J}{\partial y^2}(x_Q^I, y_Q^I)\right] u_J = 0 \quad I = 1,2,\ldots,\mathrm{NP} \tag{76}$$

where NG is the number of the Gauss quadrature points, (x_Q^I, y_Q^I), $Q = 1,2,\ldots,\mathrm{NG}$, are the Gauss quadrature points for star point I and W_g is the Gauss quadrature weight. Note that for an interpolating fixed kernel approximation, $\hat{u}_J = u_J$.

Remarks

1. In this paper, we implement the strong form local domain collocation scheme by using the interpolating shape functions for the interior points and Hermite-type approximation for the boundary points.
2. Just like the point collocation scheme, the strong form local domain collocation scheme is also a true meshless discretization scheme. However, the integration of the governing equation in the strong from local domain approach is more expensive compared to the point collocation scheme.

3.3. Weighted local domain least-squares collocation

Unlike the point collocation method, the least-squares collocation technique satisfies the governing equations in a least-squares sense at some auxiliary points as well as at the domain points [25,26]. For the governing equation given in Eq. (63), a residual norm is first defined

$$F = \sum_{I=1}^{\mathrm{NP}} [\mathscr{L}u^a(x_I, y_I) - f(x_I, y_I)]^2 + \sum_{H=1}^{NA} [\mathscr{L}u^a(x_H, y_H) - f(x_H, y_H)]^2 \quad (77)$$

where NA is the number of additional auxiliary points in the domain. Note that in [26] NA is taken to be zero. For a linear differential operator $\mathscr{L}$, substituting the fixed kernel approximation for the unknown function into the governing equation and collocating the governing equation at each domain and auxiliary point, we obtain

$$\mathscr{L}u^a(x_I, y_I) = \sum_{J=1}^{\mathrm{NP}} K_{IJ} u_J \quad I = 1, 2, \ldots, \mathrm{NP} \quad (78)$$

$$\mathscr{L}u^a(x_H, y_H) = \sum_{J=1}^{\mathrm{NP}} K_{HJ} u_J \quad H = 1, 2, \ldots, \mathrm{NA} \quad (79)$$

where K is the discrete approximation of the operator $\mathscr{L}$. For example, for the Laplace operator,

$$K_{IJ} = \frac{\partial^2 N_J}{\partial x^2}(x_I, y_I) + \frac{\partial^2 N_J}{\partial y^2}(x_I, y_I) \quad (80)$$

NP linear equations can be obtained by minimizing the residual norm given by Eq. (77)

$$\frac{\partial F}{\partial u_I} = 0 \quad I = 1, 2, \ldots, \mathrm{NP} \quad (81)$$

The linear system in Eq. (81) can be solved to find the unknown $u(x, y)$. Note that, if the differential operator $\mathscr{L}$ is nonlinear, Eq. (81) gives a nonlinear system of u_I, $I = 1, 2, \ldots, \mathrm{NP}$. Given a scattered point distribution, the location and the number of auxiliary points to use is an issue. This issue can be easily addressed if a local domain is used for least-squares minimization. This is discussed next.

Atluri et al. [4] have employed a local domain least-squares approach to minimize the residual norm in local domains. In this paper, we minimize the local residual norm by using a weighted integration form as

$$F = \int_{\Omega_s} w[\mathscr{L}u^a(x, y) - f(x, y)]^2 \mathrm{d}\Omega \quad (82)$$

where Ω_s is the local integration domain of the star point (x, y) and w is the weighting function. We construct the local integration domain Ω_s by using the approach discussed in Section 3.2. For a linear differential operator $\mathscr{L}$, minimizing Eq. (82) with respect to the unknowns u_I

$$\frac{\partial F}{\partial u_I} = 0 \quad I = 1, 2, \ldots, \mathrm{NP} \quad (83)$$

we obtain

$$\int_{\Omega_s} w[\mathscr{L}u^a(x, y) - f(x, y)] K_I(x, y) \mathrm{d}\Omega = 0 \quad (84)$$

where $K_I(x, y)$ is the discrete approximation of the operator $\mathscr{L}$ at a point (x, y). For example, for the Laplace operator,

$$K_I(x, y) = \frac{\partial^2 N_I}{\partial x^2}(x, y) + \frac{\partial^2 N_I}{\partial y^2}(x, y) \quad (85)$$

and the discretized form of Eq. (84) for a star point (x_I, y_I) can be written as

$$\sum_{Q=1}^{\mathrm{NG}} w(x_Q^I, y_Q^I) W_g(x_Q^I, y_Q^I) \left[\sum_{J=1}^{\mathrm{NP}} \left(\frac{\partial^2 N_J}{\partial x^2}(x_Q^I, y_Q^I) + \frac{\partial^2 N_J}{\partial y^2}(x_Q^I, y_Q^I) \right) u_J - f(x_Q^I, y_Q^I) \right] K_I(x_Q^I, y_Q^I) = 0 \quad (86)$$

where (x_Q^I, y_Q^I), $Q = 1, 2, \ldots, \mathrm{NG}$, are the Gauss quadrature points and W_g is the Gauss quadrature weight.

Remarks

1. The weighted local domain least-squares collocation scheme is different from the global least-squares collocation schemes [25,26] as it minimizes the residual norm in the clouds (local domains). The Gauss quadrature points of the local domains are naturally used as the auxiliary points. The weighted local domain least-squares collocation scheme is implemented by using the interpolating shape functions for the interior points and Hermite-type approximation for the boundary points.
2. As shown in the results section, the weighted local domain least-squares collocation is generally more accurate compared to the other collocation schemes discussed in this paper. However, the implementation of the least-squares collocation is more complicated and the computational cost is higher compared to other collocation schemes. Furthermore, it is only attractive for linear problems as the implementation for nonlinear problems is extremely complicated.

3.4. Double grid collocation

The basic idea in double grid collocation is to approximate the second derivatives of the unknown function $u(x, y)$ by using two subsequent first-order differentiations of the shape function [27]. In the double grid collocation technique, the second derivative of the unknown is defined as

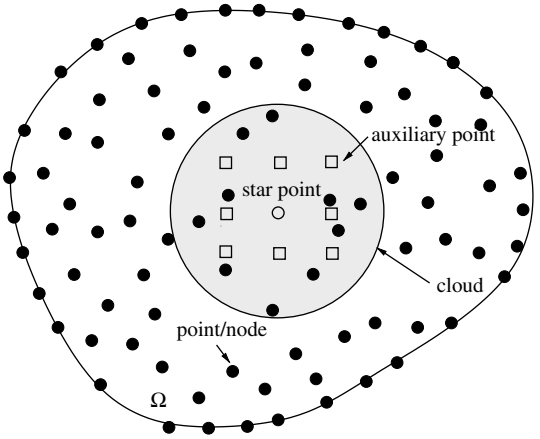

Fig. 9. A typical cloud in a double grid collocation technique.

$$\frac{\partial^2 u^a}{\partial x^2}(x,y) = \frac{\partial}{\partial x}\left(\frac{\partial u^a}{\partial x}(x,y)\right) = \sum_{I=1}^{\mathrm{NP}} \frac{\partial N_I}{\partial x}(x,y)\left(\frac{\partial u^a}{\partial x}(x_I,y_I)\right) = \sum_{I=1}^{\mathrm{NP}} \frac{\partial N_I}{\partial x}(x,y)\left(\sum_{J=1}^{\mathrm{NP}} \frac{\partial N_J}{\partial x}(x_I,y_I)u_J\right) \tag{87}$$

Eq. (87) contains two summations over two sets of first derivative approximations. The point sets I and J can either be the same or different within the cloud. Fig. 9 shows a typical double grid cloud where the auxiliary points (shown as square points) are the I points and the domain points (shown as black points) are the J points. For the Poisson equation, by using the same set of points for I and J, we substitute Eq. (87) into the governing equation to obtain

$$\sum_{I=1}^{\mathrm{NP}} \frac{\partial N_I}{\partial x}(x,y)\left(\sum_{J=1}^{\mathrm{NP}} \frac{\partial N_J}{\partial x}(x_I,y_I)u_J\right) + \sum_{I=1}^{\mathrm{NP}} \frac{\partial N_I}{\partial y}(x,y)\left(\sum_{J=1}^{\mathrm{NP}} \frac{\partial N_J}{\partial y}(x_I,y_I)u_J\right) = f(x,y) \tag{88}$$

Remarks

1. Eq. (88) is satisfied at each interior domain point by using the interpolating fixed kernel shape functions. Again, the governing equation and the boundary condition are both satisfied at the boundary points by using the Hermite-type approximation.
2. We observe that, for scattered point distributions, the solution of the double grid collocation is sensitive to the point distribution.
3. For structured point distributions, the double grid collocation technique exhibits a higher convergence rate compared to other collocation schemes for cubic base interpolating polynomial.

4. Numerical results

In this section, we first compare the performance of the boundary approximation schemes introduced in Section 2.3. Second, we compare the performance of various collocation schemes presented in Section 3 with the improvements to the fixed kernel approximation, i.e., the Kronecker delta property and the Hermite-type approximation at the boundary. A 2-D Poisson problem and several elastostatic problems are used as examples to show the numerical results. The error in the numerical solution is measured by

$$\epsilon = \frac{1}{|u^{(\mathrm{e})}|_{\max}} \sqrt{\frac{1}{NP}\sum_{I=1}^{\mathrm{NP}} [u_I^{(\mathrm{e})} - u_I^{(\mathrm{c})}]^2} \tag{89}$$

where ϵ is the error and the superscripts (e) and (c) denote, respectively, the exact and the computed solutions.

4.1. 2-D Poisson

Consider a 2-D Poisson example with a high local gradient. The governing equation along with the boundary conditions are given by

$$\frac{\partial^2 u}{\partial x^2} + \frac{\partial^2 u}{\partial y^2} = -6x - 6y - \left[\frac{4}{\alpha^2} - 4\left(\frac{x-\beta}{\alpha^2}\right)^2 - 4\left(\frac{y-\beta}{\alpha^2}\right)^2\right] \times \exp\left[-\left(\frac{x-\beta}{\alpha}\right)^2 - \left(\frac{y-\beta}{\alpha}\right)^2\right] \quad 0 \leqslant x \leqslant 1 \quad 0 \leqslant y \leqslant 1 \tag{90}$$

$$u(x=0) = -y^3 + \exp\left[-\left(\frac{\beta}{\alpha}\right)^2 - \left(\frac{y-\beta}{\alpha}\right)^2\right] \tag{91}$$

$$u,x(x=1) = -3 - 2\left(\frac{1-\beta}{\alpha^2}\right)\exp\left[-\left(\frac{1-\beta}{\alpha}\right)^2 - \left(\frac{y-\beta}{\alpha}\right)^2\right] \tag{92}$$

$$u(y=0) = -x^3 + \exp\left[-\left(\frac{x-\beta}{\alpha}\right)^2 - \left(\frac{-\beta}{\alpha}\right)^2\right] \tag{93}$$

$$u(y=1) = -x^3 - 1 + \exp\left[-\left(\frac{x-\beta}{\alpha}\right)^2 - \left(\frac{1-\beta}{\alpha}\right)^2\right] \tag{94}$$

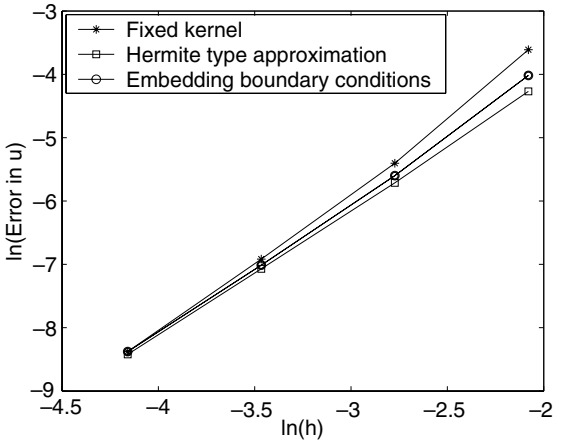

Fig. 10. Comparison of the convergence rate of the classical fixed kernel, Hermite-type approximation and the embedding boundary condition approach to treat boundary nodes for the Poisson problem.

where $\alpha = 0.2$ and $\beta = 0.5$. The exact solution for this problem is given by

$$u = -x^3 - y^3 + \exp\left[-\left(\frac{x-\beta}{\alpha}\right)^2 - \left(\frac{y-\beta}{\alpha}\right)^2\right] \tag{95}$$

To investigate the convergence rate of the various collocation schemes, the Poisson problem is solved by employing 9×9, 17×17, 33×33, and 65×65 uniformly distributed points. Fig. 10 shows a comparison of the convergence rate of the boundary approximation schemes introduced in Section 2.3. We observe that the Hermite-type approximation typically has the lowest error. Furthermore, for a 9×9 point distribution, the results from the Hermite-type approximation and the embedding boundary condition approach are significantly more accurate than the results obtained from the standard fixed kernel approximation. When 65×65 points are used, however, the results from the three techniques are quite close. Therefore, a Hermite-type approximation can produce more accurate results for coarse discretizations. The convergence plots for the four collocation schemes are shown in Fig. 11. We observe that the convergence rates of the four collocation schemes are almost the same (about 2.0). The least-squares collocation has slightly better solutions compared to the other collocation schemes. However, its computational cost is also higher. The point collocation is the simplest and fastest of the four collocation schemes.

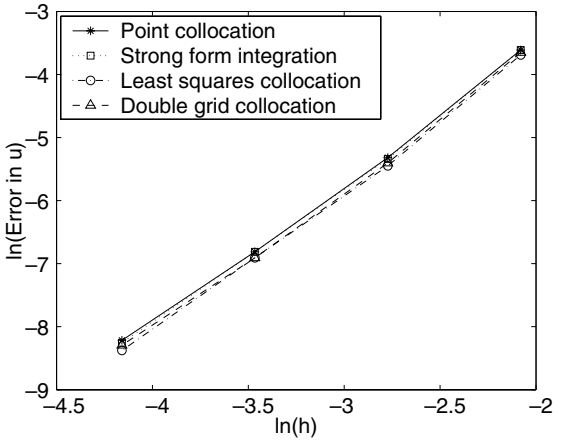

Fig. 11. Convergence rate of different collocation schemes for the Poisson problem.

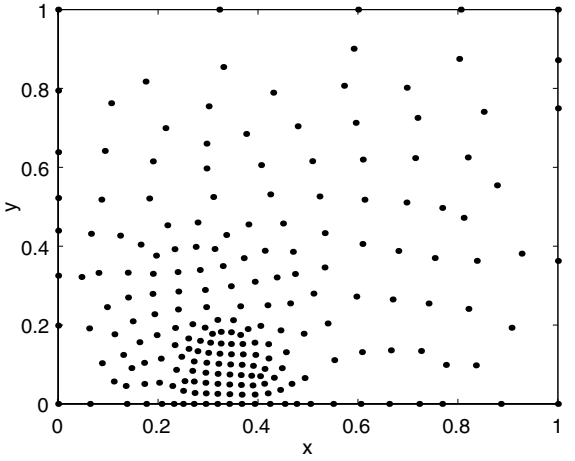

Fig. 12. 212 scattered points to solve the 2-D Poisson problem.

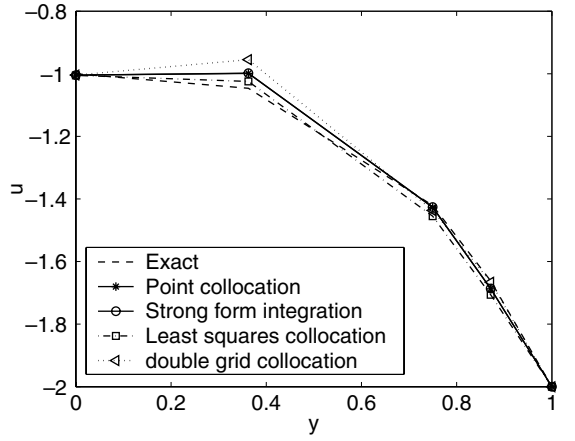

Fig. 13. Comparison of u obtained from various collocation schemes with the exact solution along the boundary $x = 1$.

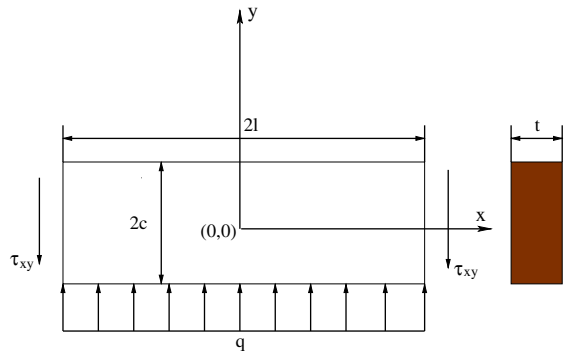

Fig. 14. A beam subjected to a uniform load and shear.

The Poisson problem is again solved by using a set of scattered points. The point distribution is shown in Fig. 12. Fig. 13 shows the solution along the boundary $x = 1$. The solution from the least-squares collocation matches well with the exact solution. The solution from the other collocation schemes is less accurate at the corner point.

4.2. 2-D Elasticity: Bending beam

The governing equations for elasticity (in a plane stress situation) are given by

$$\frac{2}{1-v}\frac{\partial^2 u}{\partial x^2}+\frac{1+v}{1-v}\frac{\partial^2 v}{\partial xy}+\frac{\partial^2 u}{\partial y^2}=0 \tag{96}$$

$$\frac{2}{1-v}\frac{\partial^2 v}{\partial y^2}+\frac{1+v}{1-v}\frac{\partial^2 u}{\partial xy}+\frac{\partial^2 v}{\partial x^2}=0 \tag{97}$$

where u and v are the x- and y-components of the displacement and v is Poisson's ratio. We consider the solution of a beam subjected to a uniform load and a shear as shown in Fig. 14. The beam is centered at (0,0), $l = 0.5$ unit, $c = 0.5$ and $t = 1$ unit. The modulus of elasticity is 3×10^3, the Poisson's ratio is 0.25 and the pressure q is 1000.

The following boundary conditions are considered

$$u(x=l,y=0)=\frac{vql}{2E}$$
$$v(x=\pm l,y=0)=0$$
$$\tau_{xy}(y=\pm c)=0$$
$$\sigma_y(y=-c)=-q$$
$$\sigma_y(y=+c)=0$$
$$\sigma_x(x=\pm l)=\frac{q}{2I}\left[\frac{2}{3}y^3-\frac{2}{5}c^2y\right]$$
$$\tau_{xy}(x=\pm l)=-\frac{q}{2I}x\left[c^2-y^2\right]$$

The exact solution for this problem is given by [28]

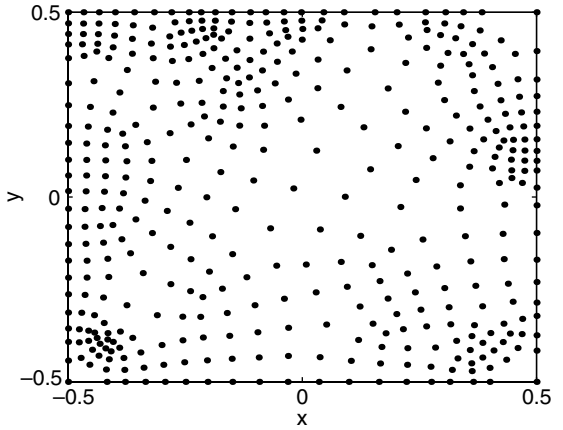

Fig. 15. The scattered point distribution employed for the bending beam problem.

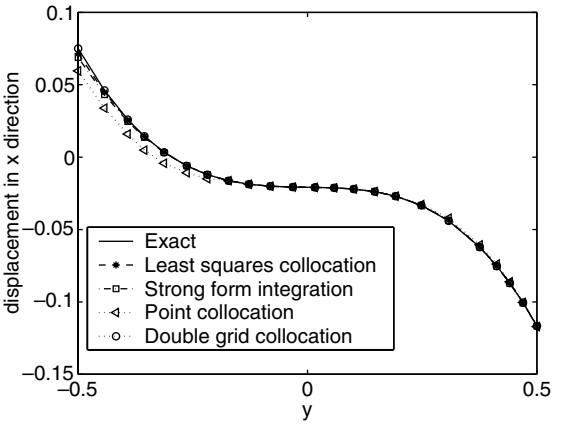

Fig. 16. The displacement in x-direction (denoted by u) along $x = -0.5$.

$$u=\frac{q}{2EI}\left\{\left[l^2x-\frac{x^3}{3}\right]y+x\left[\frac{2}{3}y^3-\frac{2}{5}c^2y\right]+vx\left[\frac{y^3}{3}-c^2y+\frac{2}{3}c^3\right]\right\}$$
$$v=-\frac{q}{2EI}\left\{\frac{y^4}{12}-\frac{c^2y^2}{2}+\frac{2c^3y}{3}+v\left[\left(l^2-x^2\right)\frac{y^2}{2}+\frac{y^4}{6}-\frac{c^2y^2}{5}\right]\right\}-\frac{q}{2EI}\left[\frac{l^2x^2}{2}-\frac{x^4}{12}-\frac{c^2x^2}{5}+\left(1+\frac{1}{2}v\right)c^2x^2\right]+\delta \tag{98}$$

$$\delta=\frac{5}{24}\frac{ql^4}{EI}\left[1+\frac{12}{5}\frac{c^2}{l^2}\left(\frac{4}{5}+\frac{v}{2}\right)\right] \tag{99}$$

This problem is solved by using a scattered point distribution of 423 points. The point distribution is shown in Fig. 15. The solution of u along $x = -0.5$ is shown in

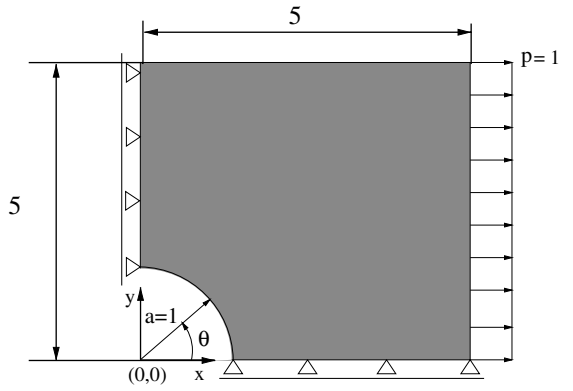

Fig. 17. Plate with a hole subjected to a uniform tensile load.

Fig. 16. The results indicate that the least-squares collocation and the strong form local subdomain collocation provide a better solution compared to the classical point collocation technique.

4.3. 2-D Elasticity: Plate with a hole

Shown in Fig. 17 is a portion of an infinite plate with a central circular hole subjected to a uniform tensile load of 1.0 in the x-direction. Due to symmetry, only a quadrant of the plate is modeled. Symmetric boundary conditions are imposed on the left and bottom edges, and the inner boundary at $a = 1$ is set to be traction-free. The Young's modulus is 1.0×10^3 and Poisson's ratio is 0.3. The exact solution for this example is given by

$$\sigma_x(x,y) = 1 - \frac{a^2}{r^2}\left[\frac{3}{2}\cos 2\theta + \cos 4\theta\right] + \frac{3a^4}{2r^4}\cos 4\theta \tag{100}$$

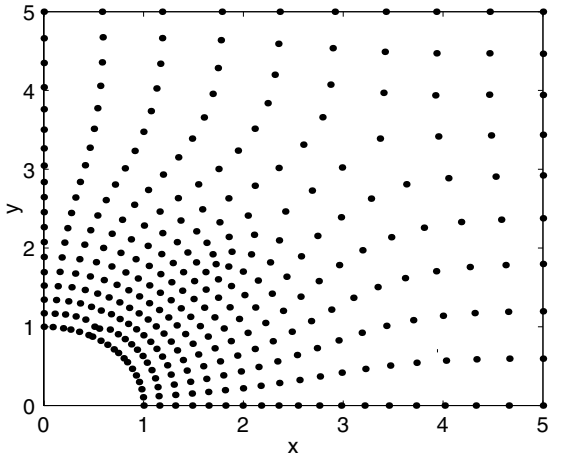

Fig. 18. The scattered point distribution employed for the plate with a hole problem.

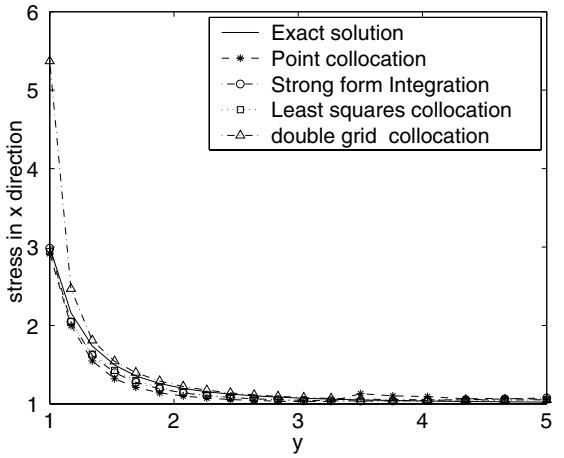

Fig. 19. The stress in the x-direction (denoted by σ_x) along $x = 0$.

$$\sigma_y(x,y) = -\frac{a^2}{r^2}\left[\frac{1}{2}\cos 2\theta - \cos 4\theta\right] - \frac{3a^4}{2r^4}\cos 4\theta \tag{101}$$

$$\sigma_{xy}(x,y) = -\frac{a^2}{r^2}\left[\frac{1}{2}\sin 2\theta + \sin 4\theta\right] + \frac{3a^4}{2r^4}\sin 4\theta \tag{102}$$

A set of 325 scattered points is used to solve the problem. The point distribution is shown in Fig. 18. The computed stress in the x-direction along $x = 0$ is compared with the exact solution in Fig. 19. We have again observed that the least-squares collocation and the strong form local domain collocation provide a better solution compared to the classical point collocation technique.

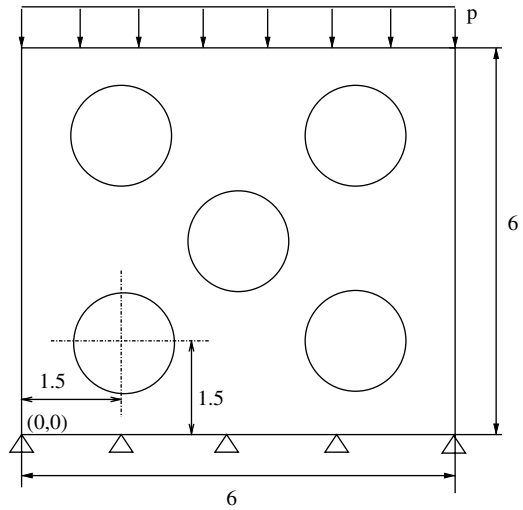

Fig. 20. A plate with several holes subjected to a uniform load on the top.

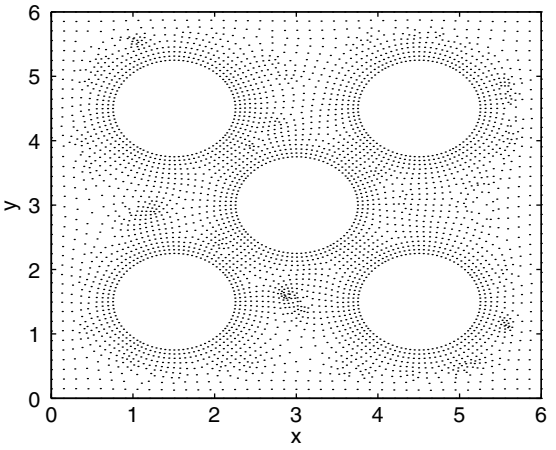

Fig. 21. The scattered point distribution employed for the plate with several holes problem.

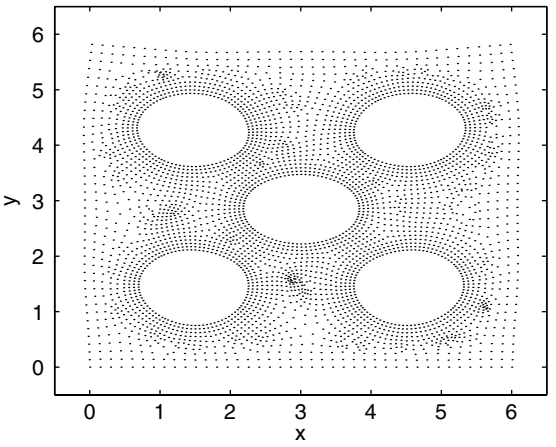

Fig. 22. The deformation of the plate.

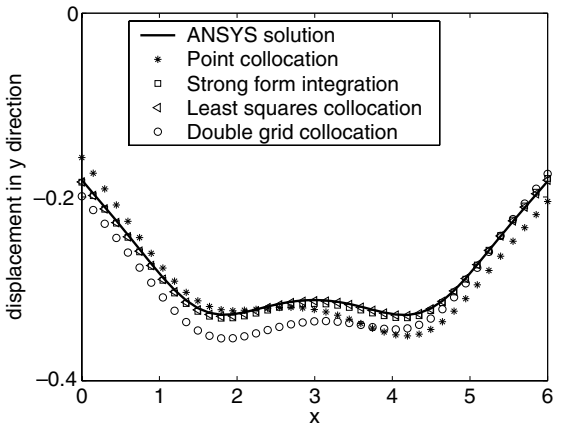

Fig. 23. The displacement in y-direction along $y = 6$.

4.4. 2-D Elasticity: Plate with several holes

An elastostatic problem with a more complex geometry is solved in this section. As shown in Fig. 20, a square plate with several circular holes is subjected to a uniform load at the top. The width of the plate is 6. The diameter of the holes is 1.5. The bottom of the plate is fixed. The pressure at the top is 1. Young's modulus is 1.0×10^3 and Poisson's ratio is 0.3.

Fig. 21 shows the point distribution employed for the plate with holes problem. The deformation of the plate is shown in Fig. 22. The displacement in the y-direction along $y = 6$ is shown in Fig. 23. We have again observed that the least-squares collocation provides a better solution compared to the other collocation schemes. The performance of the strong form local subdomain collocation is close to the least-squares collocation.

5. Conclusions

In this paper, we have proposed several improvements to the fixed kernel approximation. The improvements include the Kronecker delta property, embedding boundary condition and Hermite approach to satisfy both the governing equation(s) and the boundary condition(s) at the boundary point, and weighting coefficients to reproduce FEM stencils for large aspect ratio rectangular grids. The weighted local domain least-squares collocation scheme, the classical point collocation scheme, the strong form local domain collocation scheme and the double grid collocation scheme are implemented by combining them with the interpolating fixed-kernel shape functions for the interior points and Hermite-type approximation for the boundary points. By comparing all the collocation schemes, we have observed that, for scattered point distributions, the local domain least-squares collocation and the strong form local domain collocation are generally more accurate than the classical point collocation scheme. However, they are also more expensive. Furthermore, the implementation of the local domain least-squares collocation for nonlinear problems can be complicated. For scattered point distributions, the performance of all the collocation schemes can be improved by taking into account the positivity conditions discussed in [13].

Acknowledgement

This research was supported by the National Science Foundation under Grants CCR-9875671 and ACI-0217986. This support is gratefully acknowledged.

Appendix A. Approximation functions for high aspect ratio elasticity problem

The FEM element stiffness matrix for linear elasticity is given by

$$\int \mathbf{B}^{\mathrm{T}}\mathbf{D}\mathbf{B}\mathrm{d}x\,\mathrm{d}y \tag{103}$$

where

$$\mathbf{B} = \begin{bmatrix} N^{\mathrm{fem}}_{1,x} & 0 & N^{\mathrm{fem}}_{2,x} & 0 & N^{\mathrm{fem}}_{3,x} & 0 & N^{\mathrm{fem}}_{4,x} & 0 \\ 0 & N^{\mathrm{fem}}_{1,y} & 0 & N^{\mathrm{fem}}_{2,y} & 0 & N^{\mathrm{fem}}_{3,y} & 0 & N^{\mathrm{fem}}_{4,y} \\ N^{\mathrm{fem}}_{1,y} & N^{\mathrm{fem}}_{1,x} & N^{\mathrm{fem}}_{2,y} & N^{\mathrm{fem}}_{2,x} & N^{\mathrm{fem}}_{3,y} & N^{\mathrm{fem}}_{3,x} & N^{\mathrm{fem}}_{4,y} & N^{\mathrm{fem}}_{4,x} \end{bmatrix} \tag{104}$$

$$\mathbf{D} = \frac{E}{1-v^2}\begin{bmatrix} 1 & v & 0 \\ v & 1 & 0 \\ 0 & 0 & \frac{1-v}{2} \end{bmatrix} \tag{105}$$

where E is Young's modulus and v is Poisson's ratio. For high aspect ratio problems, the entries of $\mathbf{B}^{\mathrm{T}}\mathbf{D}\mathbf{B}$ obtained from the multiplication of the entries of the third row of $\mathbf{B}$ (shear strain) are integrated by using a reduced-order numerical integration. Basically, four kinds of terms are integrated in Eq. (103), i.e, $\int N^{\mathrm{fem}}_{i,x}N^{\mathrm{fem}}_{j,x}$, $\int N^{\mathrm{fem}}_{i,y}N^{\mathrm{fem}}_{j,y}$, $\int N^{\mathrm{fem}}_{i,x}N^{\mathrm{fem}}_{j,y}$ and $\int N^{\mathrm{fem}}_{i,y}N^{\mathrm{fem}}_{j,x}$, $i,j = 1,2,\ldots,4$. Note that for a given i and j, $\int N^{\mathrm{fem}}_{i,x}N^{\mathrm{fem}}_{j,y} \neq \int N^{\mathrm{fem}}_{i,y}N^{\mathrm{fem}}_{j,x}$. The FEM stencils are linear combinations of these integrals. We can also separate a full FEM stencil into four sub-stencils. Each sub-stencil contains only one kind of integral. It can be seen from Eq. (104) that full and reduced-order integrations are required for all the four kinds of integrations. Furthermore, the FEM stencils at the boundary nodes are different from those at the interior nodes since only two elements are involved for a boundary point. Therefore, the total number of FEM sub-stencils is 16 (four full integrations and four reduced-order integrations for both the interior nodes and the boundary nodes). We use Z to represent a full FEM sub-stencil, $\overline{Z}$ to represent a reduced-order FEM sub-stencil, I to denote an interior sub-stencil, B to denote a boundary sub-stencil, and subscripts xx, yy, xy and yx to represent the integral types. For example, an interior FEM sub-stencil containing reduced-order $\int N^{\mathrm{fem}}_{i,y}N^{\mathrm{fem}}_{j,x}$ integrations will be denoted as $\overline{Z}I_{yx}$.

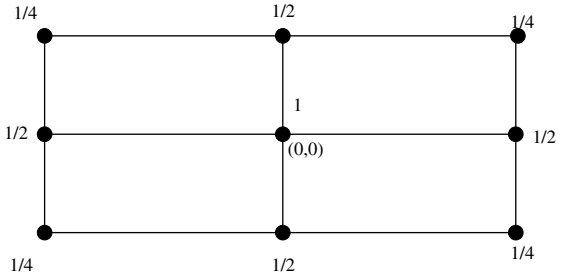

Fig. 24. FCM weighting scheme for reduced FEM integrations (interior).

It is shown that a weighting scheme of FCM shown in Fig. 4 generates interior FCM stencils for $N_{,xx}$ and $N_{,yy}$ equivalent to the FEM stencils for $\int N^{\mathrm{fem}}_{i,x}N^{\mathrm{fem}}_{j,x}$ and $\int N^{\mathrm{fem}}_{i,y}N^{\mathrm{fem}}_{j,y}$, respectively. It is easy to show that $ZI_{xy} = \overline{Z}I_{yx} = \overline{Z}I_{xy} = \overline{Z}I_{yx}$ and ZI_{yx} is also equivalent to the FCM stencil for $N_{,xy}$ generated by the weighting scheme shown in Fig. 4. Hence, by using the weighting of Fig. 4

$$N_{,xx} \approx ZI_{xx} \tag{106}$$

$$N_{,yy} \approx ZI_{yy} \tag{107}$$

$$N_{,xy} \approx ZI_{xy} = ZI_{yx} = \overline{Z}I_{xy} = \overline{Z}I_{yx} \tag{108}$$

where '≈' denotes equivalency. Moreover, without proving, $\overline{Z}I_{xx}$ and $\overline{Z}I_{yy}$ can be reproduced by FCM using the weighting scheme shown in Fig. 24. Denoting the shape functions generated by using the weighting scheme shown in Fig. 24 as R, we have

$$R_{,xx} \approx \overline{Z}I_{xx} \tag{109}$$

$$R_{,yy} \approx \overline{Z}I_{yy} \tag{110}$$

For a boundary point b, as shown in Fig. 25, the FEM stencils only contain five points in the vicinity of the point b. Therefore, only six points can be covered by a cloud for point b. Since there are only two layers of

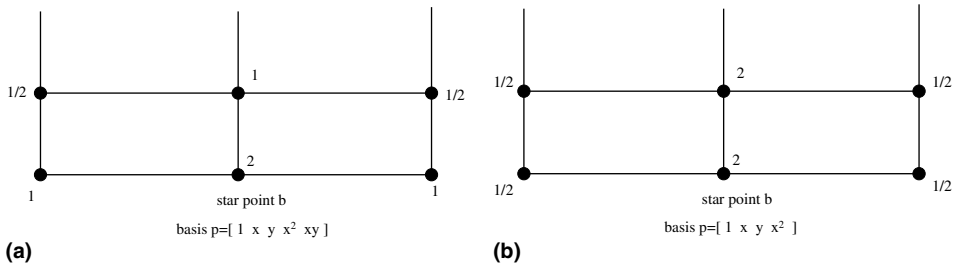

Fig. 25. Weighting schemes and reduced basis functions for boundary points.

points in the cloud, the FCM basis must be reduced to avoid singularity of the moment matrix. To reproduce the FEM stencil at a boundary point, we propose two sets of weighting schemes with reduced basis to construct the shape functions at the boundary. Fig. 25(a) shows the first set of weighting scheme and reduced basis. We denote the shape functions generated by this scheme as Q. Fig. 25(b) shows the second set of the weighting and basis. The shape functions generated by the second scheme are denoted by M. Again without proving, the special shape functions for the boundary point are equivalent to the FEM boundary sub-stencils as shown in Eqs. (111)–(116).

$$Q_{,xx} \approx ZB_{xx} \tag{111}$$

$$M_{,y} \approx ZB_{yy} \tag{112}$$

$$Q_{,y} \approx \overline{Z}B_{yy} \tag{113}$$

$$M_{,xx} \approx \overline{Z}B_{xx} \tag{114}$$

$$Q_{,xy} \approx ZB_{xy} = \overline{Z}B_{xy} \tag{115}$$

$$M_{,x} \approx ZB_{yx} = \overline{Z}B_{yx} \tag{116}$$

Eqs. (111)–(116) give all the FCM shape functions equivalent to the FEM sub-stencils. Hence, the high aspect ratio fixed-fixed beam shown in Fig. 6 can be solved by FCM to obtain properties of reduced-order shear strain FEM solution. For a given interior point (x, y), the FCM discretized governing equation is rewritten as

$$\sum_{I=1}^{\mathrm{NP}} N_{I,xx}(x,y)u_I + \frac{1-v}{2}\sum_{I=1}^{NP} R_{I,yy}u_I + \frac{1+v}{2}\sum_{I=1}^{NP} N_{I,xy}(x,y)v_I = 0 \tag{117}$$

$$\sum_{I=1}^{\mathrm{NP}} N_{I,yy}(x,y)v_I + \frac{1-v}{2}\sum_{I=1}^{\mathrm{NP}} R_{I,xx}v_I + \frac{1+v}{2}\sum_{I=1}^{\mathrm{NP}} N_{I,xy}(x,y)u_I = 0 \tag{118}$$

Note that Eqs. (117), (118) are in fact the discretized Navier's equations with the special shape functions R to represent the reduced-order FEM shear strain. For a given boundary point (x_b, y_b) located at the top or bottom of the beam, the FEM equivalent FCM stencil is given by

$$\begin{aligned}&\frac{E}{2(1+v)}\sum_{I=1}^{NP} N_{I,y}(x_b,y_b)ny_b u_I \\ &-\frac{E}{2(1-v^2)}\sum_{I=1}^{NP} N_{I,xx}(x_b,y_b)\Delta y u_I \\ &+\frac{E}{2(1+v)}\sum_{I=1}^{NP} M_{I,x}(x_b,y_b)ny_b v_I \\ &-\frac{Ev}{2(1-v^2)}\sum_{I=1}^{NP} N_{I,xy}(x_b,y_b)\Delta y v_I = T_x\end{aligned} \tag{119}$$

$$\begin{aligned}&\frac{E}{1-v^2}\sum_{I=1}^{NP} M_{I,y}(x_b,y_b)ny_b v_I \\ &-\frac{E}{4(1+v)}\sum_{I=1}^{NP} M_{I,xx}(x_b,y_b)\Delta y v_I \\ &+\frac{Ev}{1-v^2}\sum_{I=1}^{NP} M_{I,x}(x_b,y_b)ny_b u_I \\ &-\frac{E}{4(1+v)}\sum_{I=1}^{NP} N_{I,xy}(x_b,y_b)\Delta y u_I = T_y\end{aligned} \tag{120}$$

where ny_b is the unit surface outward normal of point b projected to the y axis, T_x and T_y are the x- and y-components of the surface traction.

References

[1] Aluru NR, Li G. Finite Cloud Method: a true meshless technique based on a fixed reproducing kernel approximation. Int J Numer Methods Eng 2001;50(10): 2373–410.

[2] Belytschko T, Krongauz Y, Organ D, Fleming M, Krysl P. Meshless methods: an overview and recent developments. Comput Methods Appl Mech Eng 1996;139: 3–47.

[3] Li S, Liu WK. Meshfree and particle methods and their applications. Appl Mech Rev 2002;55:1–34.

[4] Atluri SN, Shen S. The meshless local Petrov–Galerkin (MLPG) method. Tech Science Press; 2002.

[5] Jin X, Li G, Aluru NR., Meshless methods for numerical solution of partial differential equations. Handbook of materials modeling. Dordercht: Kluwer Academic Publishers [in preparation].

[6] Jin X, Li G, Aluru NR. On the equivalence between least-squares and kernel approximation in meshless msethods. Comput Model Eng Sci 2001;2(4):447–62.

[7] Oñate E, Idelsohn S, Zienkiewicz OC, Taylor RL. A finite point method in computational mechanics. Applications to convective transport and fluid flow. Int J Numer Methods Eng 1996;39:3839–66.

[8] Oñate E, Idelsohn S, Zienkiewicz OC, Taylor RL, Sacco C. A stabilized finite point method for analysis of fluid mechanics problems. Comput Methods Appl Mech Eng 1996;139:315–46.

[9] Liszka TJ, Duarte CA, Tworzydlo WW. hp-meshless cloud method. Comput Methods Appl Mech Eng 1996;139:263–88.
[10] Aluru NR. A point collocation method based on reproducing kernel approximations. Int J Numer Methods Eng 2000;47:1083–121.
[11] Oñate E, Idelsohn S. A mesh-free finite point method for advective–diffusive transport and fluid flow problems. Computat Mech 1998;21:283–92.
[12] Benito JJ, Urena F, Gavete L. Influence of several factors in the generalized finite difference method. Appl Math Model 2001;25:1039–53.
[13] Jin X, Li G, Aluru NR. Positivity conditions in meshless collocation methods. Comput Methods Appl Mech Eng 2004;193:1171–202.
[14] Belytschko T, Lu YY, Gu L. Element free Galerkin methods. Int J Numer Methods Eng 1994;37:229–56.
[15] Krongauz Y, Belytschko T. Enforcement of essential boundary conditions in meshless approximations using finite elements. Comput Methods Appl Mech Eng 1996;131:133–45.
[16] Huerta A, Fernandez-Mendez S. Enrichment and coupling of the finite element and meshless methods. Int J Numer Methods Eng 2000;48:1615–36.
[17] Breitkopf P, Rassineux A, Touzot G, Villon P. Explicit form and efficient computation of MLS shape functions and their derivatives. Int J Numer Methods Eng 2000;48:451–66.
[18] Chen JS, Han W, You Y, Meng X. A reproducing kernel method with nodal interpolation property. Int J Numer Methods Eng 2003;56:935–60.
[19] Li G, Aluru NR. Boundary cloud method: a combined scattered point/boundary integral approach for boundary-only analysis. Comput Methods Appl Mech Eng 2002;191(21–22):2337–70.
[20] Atluri SN, Cho JY, Kim H-G. Analysis of thin beams, using the meshless local Petrov–Galerkin method, with generalized moving least squares interpolations. Computat Mech 1999;24:334–47.
[21] Bathe KJ. Finite element procedures. Englewood Cliffs, NJ: Prentice-Hall; 1995.
[22] Dolbow J, Belytschko T. Volumetric locking in the element free Galekin method. Int J Numer Methods Eng 1999;46:925–42.
[23] Chen JS, Yoon S, Wang HP, Liu WK. An improved reproducing kernel particle method for nearly incompressible finite elasticity solids. Comput Methods Appl Mech Eng 2000;181:117–45.
[24] De S, Bathe K. Displacement/pressure mixed interpolation in the method of finite spheres. Int J Numer Methods Eng 2001;51:275–92.
[25] Zhang X, Liu X, Song K, Lu M. Least-squares collocation meshless method. Int J Numer Methods Eng 2001;51:1089–100.
[26] Luo Y, Haussler-Combe U. A generalized finite-difference method based on minimizing global residual. Comput Methods Appl Mech Eng 2002;191:1421–38.
[27] Breitkopf P, Touzot G, Villon P. Double grid diffuse collocation method. Computat Mech 2000;25:199–206.
[28] Timoshenko SP, Goodier JN. Theory of Elasticity. New York: McGraw-Hill; 1982.